Numerical investigations of a latent thermal energy storage for data center cooling

Zhu, Yanlong; Englmair, Gerald; Huang, Haotian; Dragsted, Janne; Yuan, Yuan; Fan, Jianhua; Furbo, Simon

Published in:
Applied Thermal Engineering

Link to article, DOI:
10.1016/j.applthermaleng.2023.121598

Publication date:
2023

Document Version
Publisher's PDF, also known as Version of record

Applied Thermal Engineering 236 (2024) 121598

Contents lists available at ScienceDirect

Applied Thermal Engineering

journal homepage: www.elsevier.com/locate/apthermeng

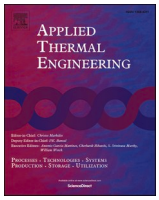

Research Paper

Numerical investigations of a latent thermal energy storage for data center cooling

Yanlong Zhu [a,b], Gerald Englmair [b,*], Haotian Huang [b,c], Janne Dragsted [b], Yuan Yuan [a], Jianhua Fan [b,*], Simon Furbo [b]

[a] School of Energy Science and Engineering, Harbin Institute of Technology, 92 West Dazhi Street, Harbin 150001, PR China
[b] Department of Civil Engineering and Mechanical Engineering, Technical University of Denmark, Koppels Allé Building 404, 2800 Kgs. Lyngby, Denmark
[c] Key Laboratory of Materials for High Power Laser, Shanghai Institute of Optics and Fine Mechanics, Chinese Academy of Sciences, 390 Qinghe Road, Shanghai 201800, PR China

ARTICLE INFO

Keywords:
Phase change material
Data center
Computational fluid dynamics
Thermal energy storage
Cold storage
Heat exchange capacity rate

ABSTRACT

The thermal performance of a 115 L latent heat storage prototype for cooling data centers was investigated. Experimentally, the heat transfer power and heat absorbed by the heat exchanger during the charging and discharging processes were measured at two flow rates (5 and 10 L/min). Numerically, two phase-change models were developed using the enthalpy and effective heat capacity methods, respectively. The results showed that the enthalpy method provides an overall better prediction of the absorbed heat, whereas the other method only agrees well with the measured results during the melting process. Thus, it is suggested that further modification of the effective heat capacity with temperature improves the agreement between the results. For a volume flow rate of 5 L/min, the average heat transfer power predicted by the enthalpy model was 2290 W during the melting process and > 920 W during the solidification process due to the smaller temperature difference for heat transfer caused by supercooling. The prototype achieved the highest average heat exchange capacity rate when melted to a 50% of its total capacity. This study provides a baseline for predicting and improving the thermal performance of latent heat storage.

1. Introduction

Globally, energy systems are undergoing a significant transition due to the decarbonization of the energy supply [1]. Renewable energy sources such as wind and sunlight can play an important role in addressing climate change [2]. However, the intermittent nature of renewable energy sources has become a major barrier to their widespread utilization. Thermal energy storage (TES) components are key to achieving high renewable energy penetration [3] by bridging the time gap between demand and production. TES can increase the power generation time and capacity factor of the electricity system [4] and store and release thermal energy for short- or long-term utilization with low heat losses [5]. Accordingly, TES has been tested and deployed in various applications such as power generation, industry, district heating and cooling, buildings, and cold chain logistics [1].

TES can be divided into sensible, latent, and chemical storage. Typically, a latent TES has a higher energy density than a sensible TES. Moreover, owing to the phase change, the latent TES can achieve a more effective heat exchange [6]. Regarding the operating temperature, latent TES is used in subzero- (<0 °C), low- (0–100 °C), medium- (100–500 °C), and high-temperature (>500 °C) applications [1]. Latent TES at low temperatures is widely deployed in cold chains and buildings, primarily for space heating, cooling, and hot water [1].

Several researchers have tested different types of latent TES systems at low temperatures. To our knowledge, shell-and-tube exchangers are the most readily available type of heat exchanger. Bourne et al. [7] investigated a latent TES unit based on a phase change material (PCM) with a melting temperature of 5 °C and found that this design increased the thermal capacity compared with a simple chilled water tank. Although the PCM was encapsulated in tubes, this unit was still classified as a shell and tube type, considering similar heat transfer methods. Likewise, Dannemand et al. [8] tested a latent heat storage unit utilizing the stable cooling of solid acetate trihydrate in the laboratory and found that the heat discharged after the solidification of the supercooled PCM was approximately 205–210 kJ/kg. Englmair et al. [9] investigated a segmented heat-storage prototype of sodium acetate trihydrate. The PCM remains in a supercooled state after releasing 30.6–34.2 MJ of

* Corresponding authors.
E-mail addresses: gereng@dtu.dk (G. Englmair), jifa@dtu.dk (J. Fan).

https://doi.org/10.1016/j.applthermaleng.2023.121598
Received 4 June 2023; Received in revised form 17 August 2023; Accepted 10 September 2023
Available online 12 September 2023

Nomenclature

Latin characters

A_{mush}	mushy zone constant, (10^5 kg/(s·m^3))
C_p	specific heat capacity, J/(kg·K)
f	liquid fraction
$\vec{F}$	body force, N/m^3
$\vec{g}$	gravitational acceleration, m/s^2
h	height of the geometry, m
h_e	sensible enthalpy, J
H	total enthalpy, J
l	length of the geometry, m
L	latent heat, kJ/kg
$\dot{m}$	mass flow rate, kg/s
N_i	element number of coarse mesh
N_j	element number of fine mesh
p	static pressure, Pa
q_s	heat flux on surface, W/m^2
Q	heat capacity, kWh
$r_{i,j}$	grid refinement factor
s	surface area, m^2
S	volume heat source, W/m^3
t	time, s
T	temperature, K
$\vec{v}$	velocity, m/s
V	volume of the geometry, m^3
$\vec{V}$	volume flow rate, m^3/s
w	width of the geometry, m

Greek symbols

δ_1	distance between the fins and container wall, m
δ_2	fin spacing, m
ε	small number to prevent division by zero, 0.001
θ	dimensional temperature
κ	thermal conductivity, W/(m·K)
ρ	density, kg/m^3

Subscripts

avg	average
ext	external
in	inlet or inside
l	liquid
max	maximum
out	outlet or outside
s	solid

Abbreviations

CFD	computational fluid dynamics
GCI	grid convergence method
HXCR	heat exchange capacity rate, W/K
NHT	numerical heat transfer
PCM	phase change material
TES	thermal energy storage

sensible heat at first. Then 31.7–37.1 MJ of latent heat was released after the solidification of the supercooled PCM was triggered. On the basis of this concept, Wang et al. [10] tested a flexible thermal energy storage filled with 137.8 kg sodium acetate trihydrate. During the discharge of the sensible heat, the heat storage can provide 294 L of hot water with an average temperature of 68.2 °C. In contrast, the latent heat could provide 334 L of hot water with an average temperature of 46.7 °C.

The thermal conductivity of PCM is typically low. To improve the heat-exchange performance, Zhang et al. [11] investigated the influence of partial and gradient filling strategies of copper foam on the heat transfer characteristics of a latent TES. When the filling ratio was 5/6, and the copper foam was placed close to the heating wall, the melting rate of the PCM reached its maximum value. Zhai et al. [12] developed a fin-tube latent TES using capric and lauric acids as PCM. According to the author, two or more fin tube units in parallel can be used to satisfy the different cold-storage demands of high-temperature cooling systems in buildings. Likewise, Behi et al. [13] investigated the heat pipe TES. The results showed that this device significantly improved the energy transfer between water and the PCM. A simple and effective way to improve the performance of the shell-and-tube heat exchanger is to arrange the fins along or normal to the pipeline. Gao et al. [14] investigated heat-storage filling using foamed copper with a radial-gradient pore density. Their results revealed that the gradient pore structure improved the uniformity of the temperature field by 4%. The solidification time was reduced by 14%. Li et al. [15] compared the melting behaviors of five innovative fin structures during heat storage, and the results showed that the tree-shaped fin exhibited the best improvement in melting time.

Compared with experimental tests, a numerical model can predict a wide range of geometries and operating conditions at minimal cost. Regarding latent TES, numerical models can typically be classified into 1-D or 2-D numerical heat transfer (NHT) [16–18] and 3-D computational fluid dynamics (CFD) models. Generally, the former is used for predicting the entire TES system, whereas the latter is used for designing and optimizing the TES. Moreover, considering the accuracy of the NHT model, the correlation between the heat transfer characteristics can be obtained based on the results of the CFD model [19].

Different methods for developing a 3-D CFD model of a latent TES exist. The enthalpy method is the most popular for modeling the melting and solidification processes. Lu et al. [20] designed a latent TES with non-uniformly distributed fins to enhance the heat transfer of the PCM. The Ansys Fluent was used to solve the phase-change process based on the enthalpy method, and the results demonstrated that, after the same time, the mass of the melted PCM in the optimized case was larger than that without any fins, which was increased by 24.5%. Liu et al. [21] established a numerical model of a latent TES with Y-shaped fins using the enthalpy-porosity method, which accelerated the melting process of the bottom part using non-uniform fins and reduced the total charging time. Likewise, Eisapour et al. [22] evaluated a novel latent TES model also based on the enthalpy method that integrated wavy and twisted tubes. This design, equipped with wavy tubes, offered nearly 83% faster charging time than the conventional design with straight tubes. Wołoszyn et al. [23] designed a helical-coiled shell-and-tube heat storage system numerically and solved it using the enthalpy method. The melting and solidification times and energy and exergy efficiencies were compared and revealed that the novel configuration achieved high overall exergy efficiency, low solidification time, and low melting time.

An effective heat capacity method can also be used to model the phase change process. Fan et al. [24] studied the energy and exergy efficiencies of a latent TES with different numbers of tubes and cascaded stages using the equivalent heat capacity method. The results indicated that a tank with four tubes and three cascaded stages exhibited the highest energy and exergy efficiencies. Iten et al. [25] compared the effective heat capacity and enthalpy methods through an experiment on an air-PCM storage unit, and the results showed that the enthalpy method predicted the phase-change stage using a quasi-horizontal curve, which is appropriate for pure PCMs. In contrast to the methods mentioned above, Chen et al. [26] developed a multiphase method for modeling the heat transfer characteristics of shell-and-tube heat storage systems. The absorption and release of heat during the phase transition

were calculated using a user-defined function. The heat content during the melting and solidification processes in the numerical model agreed well with the experimental results.

Recently, data centers have become more and more popular and consume approximately 3% of the global electric power [27]. However, the local overheating of IT equipment threatens the safe operation of data centers. In addition to the electric chillers used for cooling[28], attempts have been made to combine traditional cooling systems with latent TES to improve the flexibility and buffer capacity of the cooling system of the data center. Latent TES can provide flexibility for energy systems to integrate large shares of other renewable energy sources [29]. Furthermore, owing to the strong fluctuation in the heat load, an electric chiller should be designed to match the peak demand. As a buffer, a cooling system with latent TES can reduce the power of the electric chiller and therefore improve the system efficiency and stability[30].

Ma et al. [31] designed a system integrated with a shell-and-tube latent TES for the emergency cooling of a data center. The melting temperature of the PCM was 10–12 °C. This reveals that the proposed prototype can maintain operational servers for approximately 6 min. Huang et al. [32] proposed a ceiling air conditioner with a latent TES to alleviate the need for an uninterruptible power supply system (UPS). The shape of the heat exchanger was smooth plate containing the PCM with a phase change temperature ranging between 25 and 27 °C. The results showed that the heat storage could satisfy the cooling requirement of 300 s of emergency cooling under all working conditions. Fang et al. [33] numerically calculated a basic cooling unit with a shell-and-tube TES and evaluated the effect of the thermal conductivity of the PCM on the capacity effectiveness of the cooling system. The results showed that this novel cooling unit could provide approximately three times the thermal energy provided by the equivalent water tank. Zheng et al. [34] proposed an air-based phase-change cold storage unit for emergency cooling of a Data Center. The PCM is encapsulated in a shell plate. The results showed that rearranging the containers from in-line to staggered form, the average exergy efficiency during the discharging process has been improved by 3%.

As mentioned above, the latent TES used for data center cooling is still in its early stage, and its thermal performance must be studied and optimized. Existing studies used shell-and-tube or flat-plate heat exchangers. Owing to the requirement of data centers that the cooling system transfer heat loads quickly, it is necessary to improve the heat transfer power.

Numerical models of latent TES at low temperatures mainly use the enthalpy method or effective heat capacity method to simulate the phase change process. The advantages and disadvantages of these two methods of latent TES for datacenter cooling are unclear. In practice, thermophysical properties such as latent heat and specific heat capacity depend on the temperature and phase change state. In addition, supercooling may occur during the solidification of some PCM. This resulted in the storage and release of heat complexes. It is important to determine the method that can obtain better results than actually tested.

Accordingly, this study emphasizes the selection of a suitable CFD model of a fin-tube latent TES for datacenter cooling. The outlet temperature, absorbed heat, and heat transfer power are selected to validate the enthalpy and effective heat capacity methods developed in this study. In addition, the effect of supercooling during the solidification process is analyzed based on the heat transfer power. Finally, the heat exchange capacity rate (HXCR) of the heat storage system is determined using a CFD model. The variation in the HXCR with the status of melting or solidification is obtained to determine the optimized part-working strategy of this latent heat storage prototype. The findings of this study provide a good reference for the design and optimization of latent TES for cooling data centers.

2. Experimental method

A latent TES storage unit was tested in a heat storage test facility at the Technical University of Denmark (DTU). The heat storage unit includes 153.1 kg Rubiterm SP 15 with a phase change temperature of 15 °C enclosed in a stainless container. A tube-and-fin heat exchanger was inserted into the melting PCM. The prototype was designed to store energy from the cooling system and transfer heat loads away from the data center. The dimensions of the latent TES container were 1150 mm × 200 mm × 710 mm. Fig. 1 illustrates the details and diagram of the storage unit. Fig. 1 (a) and (b) show the heat exchanger and the exterior of the TES unit, respectively. For simplicity, this figure does not include the insulating cover. The heat exchanger consisted of stainless-steel coil tubes and aluminum fins. There were 265 parallel fins from the top to bottom of the heat-storage system. The distance between fins was 2 mm. The gap between the edge of the fins and the container wall was 35 mm. As shown in Fig. 1 (c) and (d), water passes through the coil tubes, heating or cooling the PCM in the container. There were 13 parallel tubes and channels in this unit. A tube or channel is shown as an example in Fig. 1 (c) (marked in red). In each channel, the tube is composed of a coil with a spacing of 76.6 mm. Because the hydraulic length of the tube was the same for the 13 channels, it was reasonable to assume that water was distributed uniformly among the 13 channels. Thus, the thermal performance of the entire latent TES unit can be predicted using the CFD model of a typical channel. With the exception of the two channels at both ends, a CFD model of a typical channel (subunit) was created, as shown in Fig. 1 (e). Each subunit included a coil tube with one inlet and one outlet.

Three PT100 temperature sensors are installed [35]. One was fixed 20 mm from the outside of the container wall to measure the ambient temperature. The inlet and outlet pipes of the heat exchanger (shown in Fig. 1b) were connected to the laboratory test setup using T-shaped tubes. The T-shaped tubes were specially designed so that the other two PT100 sensors inserted in the tubes were against the flow directions in the inlet and outlet pipes. The aim was to secure an accurate measurement of the temperature sensors. The piping was well-insulated around the measurement points. Fifteen copper and constantan thermocouples (Type T) (p_1–p_{15}) were installed at different positions, as illustrated in Fig. 2 [35]. Thermocouples p_1 and p_2 were used to measure the ambient temperature, which is not shown in the figure. p3–p8 were arranged between the two fins and immersed 25 mm from the edge of the fins. p_3–p_5 recorded the temperatures at the outlet side, whereas p_6–p_8 recorded the temperatures at the inlet side. Additionally, p_9–p_{13} were distributed in the gap between the fins and walls of the container in the vertical direction. Temperatures at the top and bottom of the storage container were measured at p_{14} and p_{15}, respectively. The maximum measurement uncertainty is ± 0.1 K for the PT 100 temperature sensors and ± 0.4 K for the thermocouples. In terms of the volume flow rate, two Kamstrup flowmeters were used with a measurement uncertainty of ± 1% [36].

A constant inlet temperature was maintained using the laboratory test setup. Inlet temperatures applied during the melting process is 25 °C, which is the required temperature of data center. Inlet temperatures applied during the solidification process is 9 °C, which is the design temperature of cooling system. The volume flow rates applied in the test cycles were 5 and 10 L/min.

3. Numerical method

3.1. Geometry and mesh

To reduce the computing resource requirements, it is necessary to simplify the geometry. There were 13 parallel channels in total in the latent TES unit, and the distributor at the top of the storage container distributed the water uniformly. A typical channel was selected to represent the entire unit, as shown in Fig. 1 (e). The thicknesses of the tubes and fins were 2 mm and 0.1 mm respectively. The tube was 16.2 mm. The main assumptions of this study are as follows.

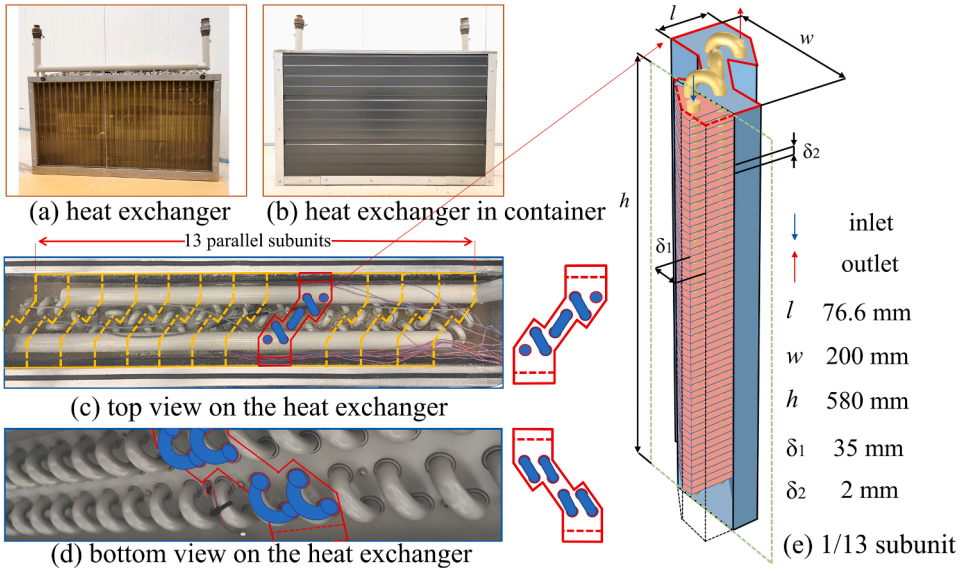

Fig. 1. The details and diagram of the latent TES for data center cooling. (a) Heat exchanger with fins. (b) The heat exchanger in container. (c) The top view on the heat exchanger. (d) The bottom view on the heat exchanger. (e) The diagram of the subunit used in the numerical model.

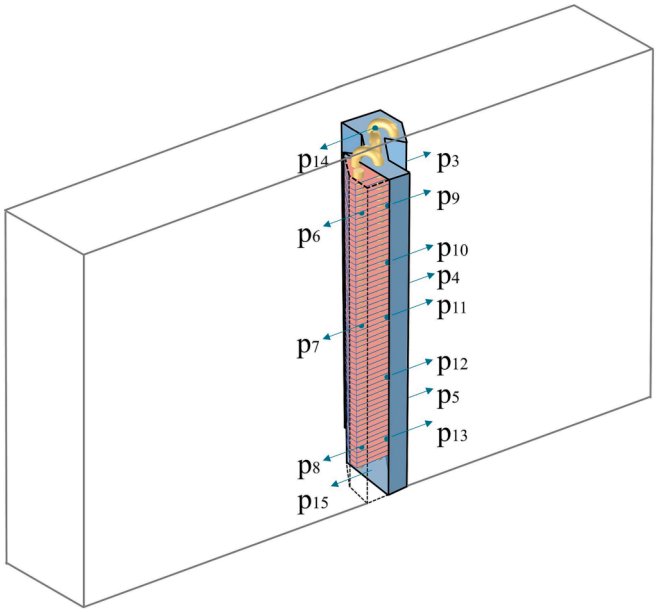

Fig. 2. The positions of the different thermocouples in the storage prototype.

(1) The 13 parallel channels have the same thermal conditions, neglecting the effects of the two ends of the heat exchanger.
(2) The thickness of the container wall is neglected due to the following reasons. Firstly, the number of mesh elements including walls is much larger than that without walls, which is difficult to solve. Secondly, the container wall was made of steel with a thermal conductivity much higher than that of the PCM. Therefore, it was reasonable to disregard the temperature difference between the inner and outer surfaces of the container wall. A method for calculating the heat transfer resistance on both sides of a wall is introduced in Section 3.2. Moreover, the thermal capacity of the container wall was considered to be the total heat capacity of the PCM based on the total mass and specific heat capacity of the container wall.
(3) The volume flow rate of the heat transfer fluid was equal to or lower than 10 L/min. The Reynolds number Re corresponding to the maximum volume flow rate (10 L/min) was approximately 1550, which is lower than the turbulent transition threshold (2400); therefore, the flow was considered incompressible and laminar.
(4) The Boussinesq approximation was used to calculate the effect of natural convection during the PCM melting. The density was constant in all solved equations, except for the buoyancy term in the momentum equation [37].
(5) The material properties of the PCM except specific heat capacity are constant.

Fig. 3 shows the mesh used in this study. A hybrid mesh with structured and unstructured elements was generated using Ansys® Mesher, Release 2020R1. Fig. 3 (a) and (b) show the meshes at the top and bottom of the storage, respectively. Fig. 3 (c) shows a sweep mesh along the direction of the fin array. Three mesh schemes with 705678, 1547701, and 3,680,035 elements were generated to validate the mesh

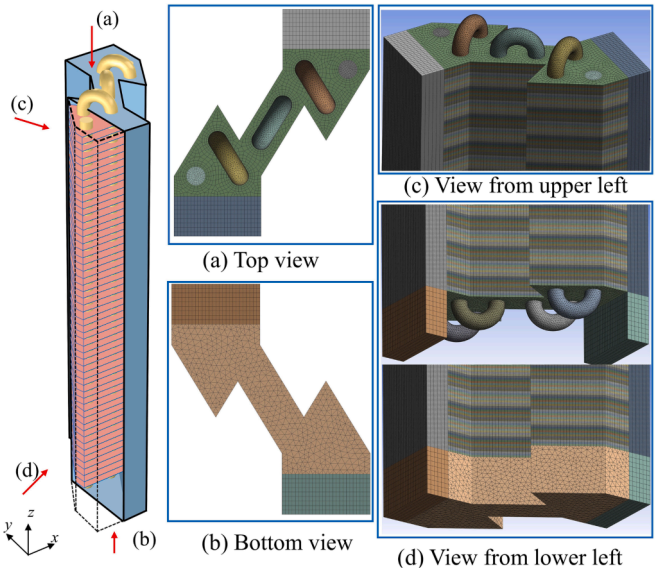

Fig. 3. The details of the mesh of the cold storage. (a) The top view, (b) the bottom view, (c) the view from upper left, and (d) the view from lower left.

independence (see Section 3.6).

3.2. Boundary conditions and materials properties

Because the simplified CFD model represents 1/13 of the entire storage unit, a translation-periodic boundary condition was adopted at the interfaces between the subunits, as shown in Fig. 3 (c).

The heat loss coefficient on the wall of the subunit was considered by:

$$U = \frac{1}{R_{si} + R + R_{se}} \tag{1}$$

where, R_{si} (0.1 m^2·K/W) is the thermal resistance between the PCM and container wall, and R_{se} (0.14 m^2·K/W) is the external thermal resistance between the insulation and environment. R is the thermal resistance of the container wall and insulation and is defined as

$$R = \frac{\delta_c}{\lambda_c} + \frac{\delta_{ins}}{\lambda_{ins}} \tag{2}$$

where δ_c (0.002 m) and δ_{ins} (0.05 m) are the thicknesses of the container wall and insulation, respectively. λ_c (70.2 W/(m^2·K)) and λ_{ins} (0.04 W/(m^2·K)) are the thermal conductivities of the container wall and insulation, respectively. The heat loss coefficient was adopted as 0.65 W/(m^2·K), respectively. The wall thermal conditions are defined as follows:

$$-k\frac{\partial T}{\partial n_w} = U(T_a - T_w) \tag{3}$$

The volume flow rates of the water were 5 and 10 L/min, which were the same as those in the experiment. According to the design temperatures of data center and cooling system, the heat storage prototype should work between 9 °C and 25 °C. The numerical simulation started with an initial temperature, 9 °C of the storage unit, which was heated by the water with an inlet temperature of 25 °C. When all PCM melted, the melting process was considered. The solidification process started immediately by switching the inlet temperature to 9 °C until all the PCM solidified again. The inlet temperatures were used as follows:

$$T_{in} = \begin{cases} 25\ ^\circ\text{C melting} \\ 9^\circ\text{C solidification} \end{cases} \tag{4}$$

Table 1 lists materials properties used in the model including the PCM, water, steel tubes and aluminum fins. The material properties of the PCM are supported by the data from Rubitherm [38]. The data mentions that the PCM has a high viscosity in the liquid state, without accurate value. Thus, a large viscosity value was selected. The sensitivity study on viscosity should be added in future work.

The storage prototype consisted of a container, insulation covering all sides, a heat exchanger, water in coil pipes, and a PCM in the container. Table 2 lists the weights and heat capacities of storage components. The heat capacity was evaluated according to the specific heat capacity in the temperature range of 9–25 °C. The data in the table indicate how each component is considered in the numerical model.

Table 1
Materials properties used in the model.

Property	SP15 [38]	water [26]	steel	Al
Density, (kg/m^3)	1375	784 + 1.6595 T-0.0032 T^2	7870	2700
Specific heat capacity, (J/(kg·K))	2000	5641–9.1467 T + 0.0143 T^2	440	900
Thermal conductivity, (W/(m·K))	0.6	−0.3222 + 0.0046 T-5 × $10^{-6}T^2$	70.2	238
Viscosity, (Pa·s)	10.3	5 × $10^{11}T^{-5.954}$		
Heat of fusion, (kJ/kg)	155	–		
Melting temperature, (°C)	15–17	–		
Solidification temperature, (°C)	10–12	–		

Table 2
The weight and heat capacity of each component of the storage prototype.

Component	Weight, (kg)	Heat capacity (kWh) (9–25 °C)	If modeled?
Empty container	52.0	0.1	Converted into PCM
Heat exchanger	39.7	0.16	Yes
Insulation cover	5.8	–	Measured heat loss coefficient
Water in coil pipe	13.1	0.24	Yes
PCM in container	153.1	7.23	Yes

The commercial computational fluid dynamic (CFD) software Ansys® Fluent, release 2020R1, was used to set up the numerical model. SIMPLEC was employed as the pressure–velocity coupling scheme. The spatial discretization methods of the pressure, momentum, and energy equations were based on second-order, first-order upwind, and second-order upwind schemes, respectively. The time discretization method is a first-order implicit scheme. Calculations were performed based on high-performance clusters (HPC) at the DTU [39].

3.3. The enthalpy method

The default enthalpy method was implemented using the solidification and melting model in Fluent. Instead of tracking the liquid–solid front explicitly, the liquid fraction, which indicates the fraction of the cell volume in the liquid form, is associated with each cell in the domain. The liquid fraction of each cell was calculated using the governing equations. A mushy zone was introduced in the cells where the liquid fraction was between 0 and 1. The governing equations are as follows [40]:

Continuous equation:

$$\frac{\partial \rho}{\partial t} + \nabla\cdot(\rho\vec{v}) = 0 \tag{5}$$

Momentum equation:

$$(\rho\vec{v}) + \nabla\cdot(\rho\vec{v}\vec{v}) = -\nabla p + \nabla\cdot(\bar{\bar{\tau}}) + \rho\vec{g} + \vec{F} \tag{6}$$

$$\vec{F} = \frac{(1-f)^2}{(f^3+\varepsilon)}A_{mush}\vec{v} \tag{7}$$

Energy equation:

$$\frac{\partial}{\partial t}(\rho H) + \nabla\cdot(\rho\vec{v}H) = \nabla\cdot(k\nabla T) + S \tag{8}$$

where f is the liquid volume fraction:

$$f = \begin{cases} 0 & T < T_s \\ \dfrac{T - T_s}{T_l - T_s} & T_s < T < T_l \\ 1 & T > T_l \end{cases} \tag{9}$$

where subscript s represents the solid and l represents the liquid.

In eq. (7), ε is a small number (0.001) to prevent division by zero [40], A_{mush} is the mushy zone constant (10^5 default values used in Fluent). Small values of A_{mush} result in unrealistic predictions, whereas large values of A_{mush} results in delayed predictions [41]. H is the enthalpy, defined as

$$\begin{aligned} H &= h + \Delta H \\ \Delta H &= fL \end{aligned} \tag{10}$$

where L is the latent heat of the PCM. According to the definition of liquid fraction and enthalpy, the latent enthalpy, ΔH, remains a linear

function with temperature.

3.4. The effective heat capacity method

For the effective heat capacity method, the same equations as mentioned above were used. The basic difference between the two methods is that the effective heat capacity method converts the latent enthalpy into a sensible enthalpy by defining the effective specific heat capacity with respect to temperature, which can be defined as

$$\begin{array}{ll} C_{p,s} & T < T_s \\ 0.5 \times C_{p,s} + 0.5 \times C_{p,l} + f(T)L & T_s < T < T_l \\ C_{p,l} & T > T_l \end{array} \tag{11}$$

where $f(T)$ is a temperature-dependent function that converts latent heat to a specific heat capacity. Thus, enthalpy remains a user-defined function with temperature. Different functions of this method have been implemented in previous studies. It is shown that using the experimental data measured by DSC is more suitable than using other functions such as square-wave and Gaussian functions [42]. In this study, the function was fitted according to the partial enthalpy distribution measured using Rubitherm, which was shown in Table 3 [38].

3.5. Parameters used for model verification and comparison

The parameters used for model verification and comparison were determined as follows:

The absorbed heat by the heat exchanger was defined as:

$$\begin{aligned} Q_{abs} &= \int_0^t q_{abs} \\ &= \int_0^t \dot{m} C_p (T_{out} - T_{in}) \end{aligned} \tag{12}$$

where q_{abs} is the heat transfer power (W); $\dot{m}$ is the mass flow rate (kg/s); T_{out} and T_{in} are the water temperatures at the inlet and outlet, respectively. Because the temperature difference between the storage prototype and the ambient environment was small, the heat loss was not important for calculating the heat absorbed by the heat exchanger.

The absorbed heat by the heat exchanger can also be calculated by:

$$Q = \int_{S_{out}} q_{s,out} ds - \int_{S_{inner}} q_{s,in} ds \tag{13}$$

where $q_{s,in}$ and $q_{s,out}$ are the heat fluxes on the surfaces of the inner and outer tubes, respectively.

A GCI grid error analysis [43] was implemented to estimate the discretization error, in which only three meshes were required. r_{21} and r_{32} represent the ratios of the mesh sizes, which are defined as

$$r_{i,j} = \sqrt[3]{\frac{V}{N_i}} \Big/ \sqrt{3\frac{V}{N_j}} \tag{14}$$

where N_i and N_j denote the element numbers of the coarse and fine meshes, respectively. V is the total volume of the subunit.

Moreover, θ_{out} is the dimensionless temperature of the outlet, defined as:

Table 3
Partial enthalpy distribution of the PCM [38].

T (°C)	Partial enthalpy (kJ/kg)	T (°C)	Partial enthalpy (kJ/kg)
7	4	15	10
8	4	16	72
9	5	17	14
10	4	18	10
11	6	19	7
12	6	20	9
13	7	21	8
14	10	22	11

$$\theta_{out} = \frac{T_{out} - T_{in}}{T_{out,final} - T_{in}} \tag{15}$$

θ_{ext} is the extrapolated value estimated using this method, which corresponds to an infinite mesh.

GCI is the discretization error, defined as:

$$GCI^{21} = \frac{1.25\left|\frac{\theta^1_{out} - \theta^2_{out}}{\theta^1_{out}}\right|}{r_{21}^n - 1} \tag{16}$$

where n is apparent order, defined as:

$$n = \frac{1}{\ln(r_{21})}\left|\ln\left|\frac{\theta^3_{out} - \theta^2_{out}}{\theta^2_{out} - \theta^1_{out}}\right| + \ln\left(\frac{r_{21}^n - sgn(\theta^3_{out} - \theta^2_{out})}{r_{32}^n - sgn(\theta^2_{out} - \theta^1_{out})}\right)\right| \tag{17}$$

The heat exchange capacity rate (HXCR) was determined by:

$$HXCR = -\rho C_p \dot{V} \cdot \ln\left(1 - \frac{T_{in} - T_{out}}{T_{in} - T_{avg,PCM}}\right) \tag{18}$$

where T_{in} and T_{out} are the inlet and outlet temperatures of the water, $T_{avg,PCM}$ are the average temperatures of the PCM in the storage unit, which were obtained directly using Fluent. The HXCR indicates the heat transfer ability, depending on the temperature difference.

The heat transfer power can be calculated by:

$$q = \rho C_p \dot{V} (T_{in} - T_{out}) \tag{19}$$

The energy-weighted heat transfer power and HXCR were defined as:

$$\phi_{avg} = \int_0^{Q_{max}} Q\phi dQ \tag{20}$$

where ϕ denotes the heat transfer power or HXCR, Q denotes the heat content of the storage unit, and Q_{max} denotes the total heat capacity of the storage unit.

3.6. Parameter selection

The key parameters and mesh independence were examined using both methods. For brevity, only the enthalpy method results are presented in this section.

A. Time step sizes.

Fig. 4 shows the heat absorbed by the heat exchanger at a volume flow rate of 5 L/min with seven different time-step sizes. All the simulations converged.

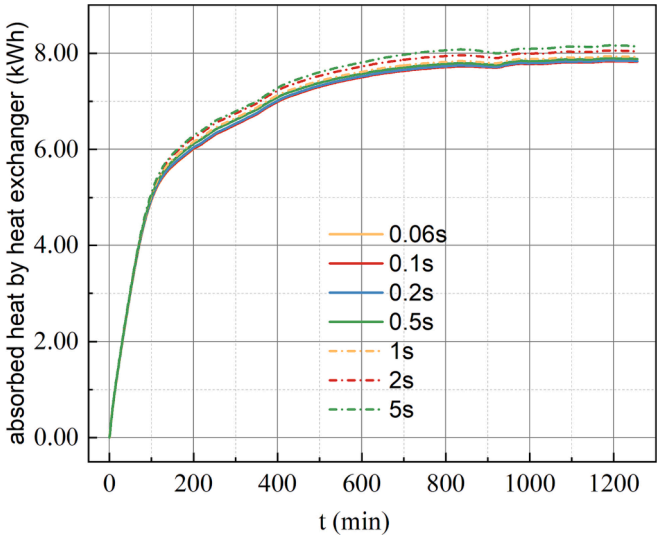

Fig. 4. The absorbed heat by the heat exchanger during the melting process in different times.

For the time-step sizes of 0.06, 0.1 s and 0.2 s, the absorbed heat by the heat exchanger during the melting process almost overlapped each other. For time steps of 0.5 s and 1 s, the heat absorbed by the heat exchanger was slightly different from that of the time step 0.06 s. The maximum difference was 0.0175 kWh. However, compared with the result at 0.06 s, the maximum differences for the time steps of 2 s and 5 s were 0.028 kWh and 0.043 kWh, respectively. Therefore, 1 s was selected as the optimal time step.

B. Under-relaxation factor.

To explore the optimal relaxation factor, a series of under-relaxation factors were used, and the results are shown in Fig. 5. In comparison with the result with an under-relaxation factor of 1 (default value), the maximum differences in the heat absorbed by the heat exchanger were 0.111, 0.043, and 0.018 kWh for under-relaxation factors of 0.8, 0.9, and 0.95, respectively.

Although all these simulations converged, a small under-relaxation factor yielded false solutions. To explore the effect of the under-relaxation factor on the reliability of the solutions, the heat absorbed by the heat exchanger during the melting process was calculated using three methods. The first and second methods are based on Eqs. (12) and (13), respectively. The third method involves directly reading the enthalpy change in Fluent. The results obtained using the three methods were similar. Fig. 6 illustrates the enthalpy change in the PCM with different under-relaxation factors. When the factor was 1.0, the heat absorbed by the heat exchanger using the three methods overlapped completely during the entire melting process. However, at a factor of 0.8, the difference in the absorbed heat increased with time. This reveals that the smaller the under-relaxation factor, the larger is the difference in the absorbed heat obtained using the three methods. Because the smaller factor made the solution difficult to converge. As shown in Figs. 5 and 6, when the under-relaxation factor was 0.95 or 1, the simulation was reliable. For better convergence, an under-relaxation factor of 0.95 was selected.

C. Mesh independence.

The independence of the mesh was investigated using GCI analysis. In this analysis, only three-mesh results are required. More details can be found in theoretical research on GCI [43]. Three meshes with 705,678 (mesh 1), 1,547,701 (mesh 2), and 3,680,035 (mesh 3) elements were generated to validate mesh independence. Table 4 lists the main parameters used for the mesh independence validation. As it is shown, the discretization error at the beginning was 8.6%, it became smaller than 3% over time.

Fig. 7 shows the extrapolated dimensionless temperatures of the outlet. According to the discretization error analysis, the mesh with 3,680,035 elements was selected.

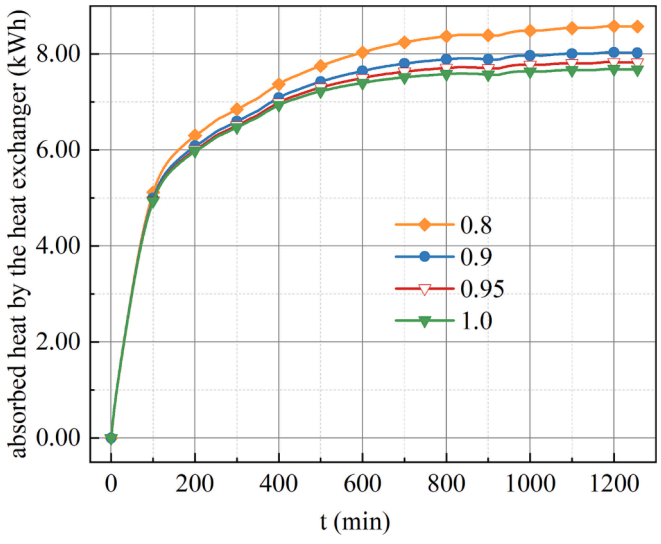

Fig. 5. The absorbed heat by the heat exchanger during the melting process in different under-relaxation factors.

4. Results and discussions

4.1. Comparison of the two phase change models

A. The results of the enthalpy method.

Fig. 8 shows a comparison between the calculated and measured outlet temperatures. The simulation results agree well with those of the experiments during the melting process. During the solidification process, there was a difference, particularly in the range of 1300–2100 min.

During the experimentally measured solidification, the outlet temperature first decreased and then increased slightly for approximately 400 min and then decreased again until the solidification process was completed, which indicated that supercooling occurred during this period. However, Fluent cannot be used to model supercooling. Therefore, the predicted outlet temperature continuously decreased.

For the entire storage cycle, the maximum difference between the predicted and the measured outlet temperature was 4.5 K. In addition to supercooling, there were other reasons for the difference between the simulation and experiment. First, the initial temperature of the storage unit was nonuniform because of pre-cooling before the melting process in the experiment, whereas the average temperature was adopted in the simulation. Second, the viscosity of the PCM is highly temperature dependent; however, an estimated constant viscosity was used in this model. Thus, the effect of natural convection during melting may have been overestimated in some periods and underestimated in others. Consequently, the predicted temperatures deviate from the measured temperatures.

Fig. 9 compares the heat absorbed by the heat exchanger in the simulation and experiment at a volume flow rate of 5 L/min. The experiments showed that the heat absorbed by the heat exchanger was approximately 8 kWh. The maximum difference between the predicted and the measured absorbed heat were 8% during the melting process and 8.5% during the solidification process. Moreover, the differences between the predicted and the measured absorbed heat using the enthalpy method were 1.4% and 1.5% at the end of the melting and the solidification processes, respectively.

The heat transfer power of the heat storage unit was also investigated. Fig. 10 (a) and (b) show that the heat transfer powers calculated using the enthalpy method agree well with those of the experiment. As shown in Fig. 10 (b), the heat transfer powers of the enthalpy method were larger than those of the experiment at 100–400 min and smaller at 400–800 min after the start of the solidification process. The heat transfer power was lower during 0–100 min because the specific heat capacity was a constant and smaller than the actual value. According to eq. (20) with a volume flow rate of 5 L/min, the energy-weighted average heat transfer power was 2290 W for the melting process and 920 W for the solidification process.

B. The results of the effective heat capacity method.

Fig. 11 shows a comparison of the outlet temperature of the effective heat capacity method and that of the experiment at a volume flow rate of 5 L/min. For the entire storage cycle, the maximum difference between the predicted and measured outlet temperature was 1.7 K using the effective heat capacity method. This reveals that this method can predict a better outlet temperature than the enthalpy method because of the specific heat capacity function fitted using the method described in Section 3.4. Fig. 12 shows the specific heat capacity fitted according to the data measured using the Rubitherm.

Fig. 13 shows a comparison of the heat absorbed by the heat exchanger using the effective heat capacity method and an experiment with a volume flow rate of 5 L/min. In the effective heat capacity method, the maximum difference during the melting process was 6%, whereas it reached 22.7% during the solidification process. Owing to supercooling, solidification in the experiment occurred anywhere it

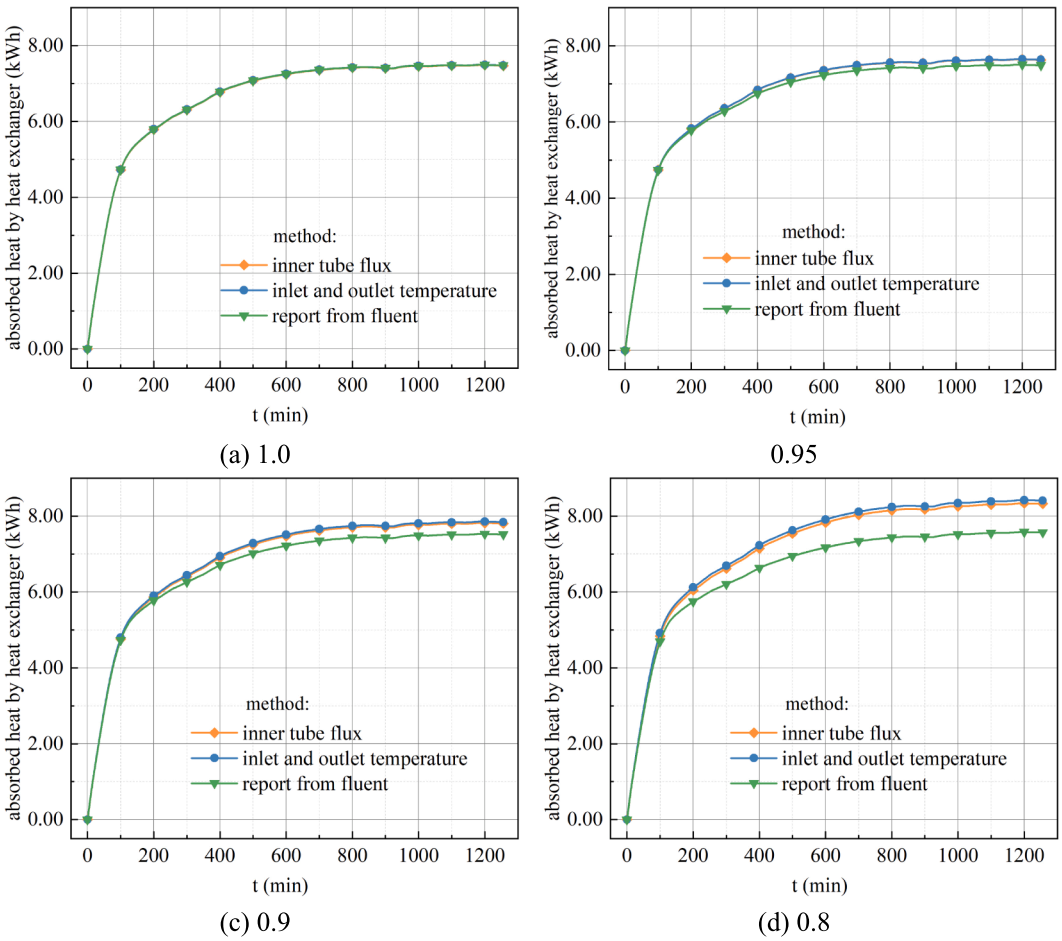

Fig. 6. The absorbed heat by the heat exchanger calculated using different methods.

Table 4
Grid convergence index analysis.

t, (min)	r_{21}	r_{32}	$\theta_{out,\ 1}$	$\theta_{out,\ 2}$	$\theta_{out,\ 1}$	$\theta_{ext,\ 12}$	GCI^{21}
10	1.34	1.30	0.284	0.294	0.287	0.265	8.6%
20	1.34	1.30	0.414	0.424	0.418	0.398	4.8%
40	1.34	1.30	0.513	0.519	0.516	0.507	1.6%
60	1.34	1.30	0.597	0.600	0.596	0.584	2.6%

reached the supercooling temperature, resulting in a continuous decrease in absorbed heat at a rather stable pace. Lacking the capability to model supercooling, the speed of the decrease in the absorbed heat became increasingly slower. The other reason was that the difference between the inlet and outlet temperatures was small in the time range from 1300 min to 2250 min. Although the predicted outlet temperature using the effective heat capacity method agreed well with that of the experiment, the small temperature difference still had a significant effect on the heat content calculation.

Moreover, the differences between the predicted and measured heat absorbed by the heat exchanger obtained using the enthalpy method are smaller than those obtained using the effective heat capacity model. In conclusion, the enthalpy method provided a better prediction of the heat absorbed by the heat exchanger of the storage unit.

The heat transfer power of the heat storage unit was also investigated. This is shown in Fig. 14 (a) and (b), respectively. During the solidification process from 0 to 400 min, the heat transfer power of the effective heat capacity method was higher than that of the experiment. This is the reason for the larger difference in the absorbed heat during this period, as illustrated in Fig. 13.

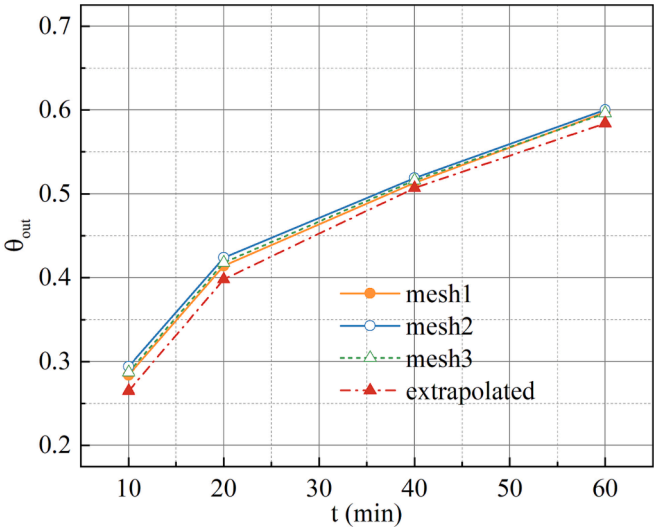

Fig. 7. The dimensionless temperature of the outlet of three meshes and extrapolated value.

A comparison of the outlet temperature, absorbed heat, and heat transfer power revealed that the model based on the effective heat capacity method predicted better local benefits from the effective C_p fitted. However, the global maximum difference in this method was larger owing to the lack of a supercooling model. The relationship between the effective specific heat capacity and temperature directly affected the

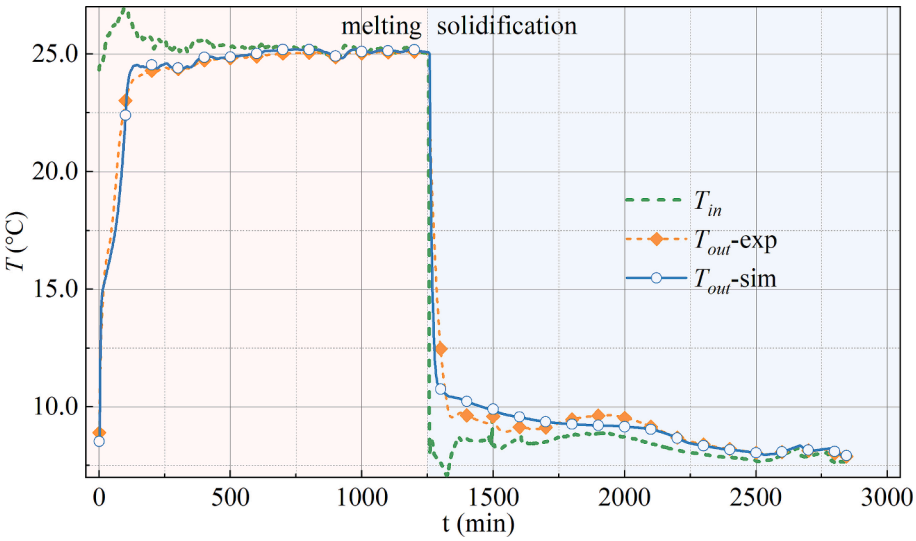

Fig. 8. The outlet temperature of the results of experiment and the enthalpy method with a flow rate of 5 L/min.

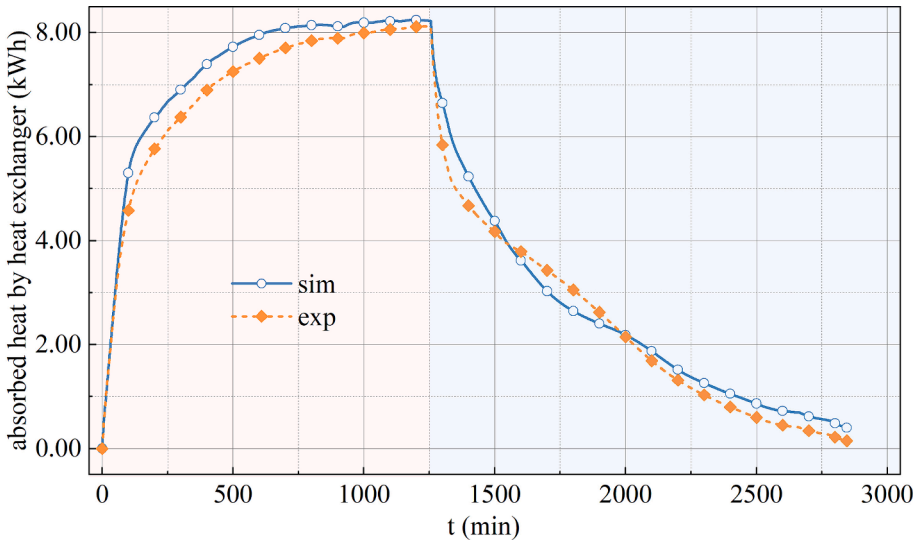

Fig. 9. The absorbed heat by the heat exchanger using the enthalpy method with the volume flow rate of 5 L/min.

results. The results demonstrate that the data measured by Rubitherm agree well with the experimental results during the melting process. Therefore, it is necessary to obtain a more accurate heat capacity distribution by considering supercooling. Although the enthalpy method has a similar problem, the smaller heat transfer power at the beginning of the solidification process can reduce the difference resulting from the larger heat transfer power compared with that in the experiment. Thus, the results of the enthalpy method agree better with the overall experimental results. Consequently, the enthalpy method was used in the subsequent experiments.

4.2. Method validation with variation of volume flow rate

In addition to the results for the 5 L/min volume flow rate, a 10 L/min volume flow rate was simulated and tested in the experiment. Fig. 15 shows the outlet temperature and heat absorbed by the heat exchanger over time. The calculated results at a volume flow rate of 10 L/min agreed well with the experimental results. The heat absorbed by the heat exchanger at the end of the melting and solidification processes was nearly identical to that in the experiment.

At a volume flow rate of 10 L/min, the thermal energy stored during the melting process was 8 kWh independent of the volume flow rate. The prototype required 918 min for complete charging. The melting time was shorter than that at 5 L/min (1256 min) because an increase in the water flow rate enhanced the heat transfer of the tubes. Although the solidification test was not completed in the case of 10 L/min, the solidification time was 650 min, whereas the case with 5 L/min required 950 min to reach the same amount of heat absorbed by the heat exchanger.

Fig. 16 shows the predicted and measured heat transfer powers at a volume flow rate of 10 L/min. Owing to the higher velocity of the water in the tube, the heat transfer power during the main time period, 0–100 min for the melting process and 0–400 min for the solidification process, varied in the range of 500–5000 W. The energy-weighted average heat transfer powers were 3370 and 1470 W at a volume flow rate of 10 L/min. An increase in the water volume flow rate increased the average heat transfer power by 47% and 59%.

4.3. Heat exchange capacity rate (HXCR) with different flow rates

Fig. 17 shows the HXCR during melting at different volume flow rates. Latent heat storage may start or end in a non-fully charged state,

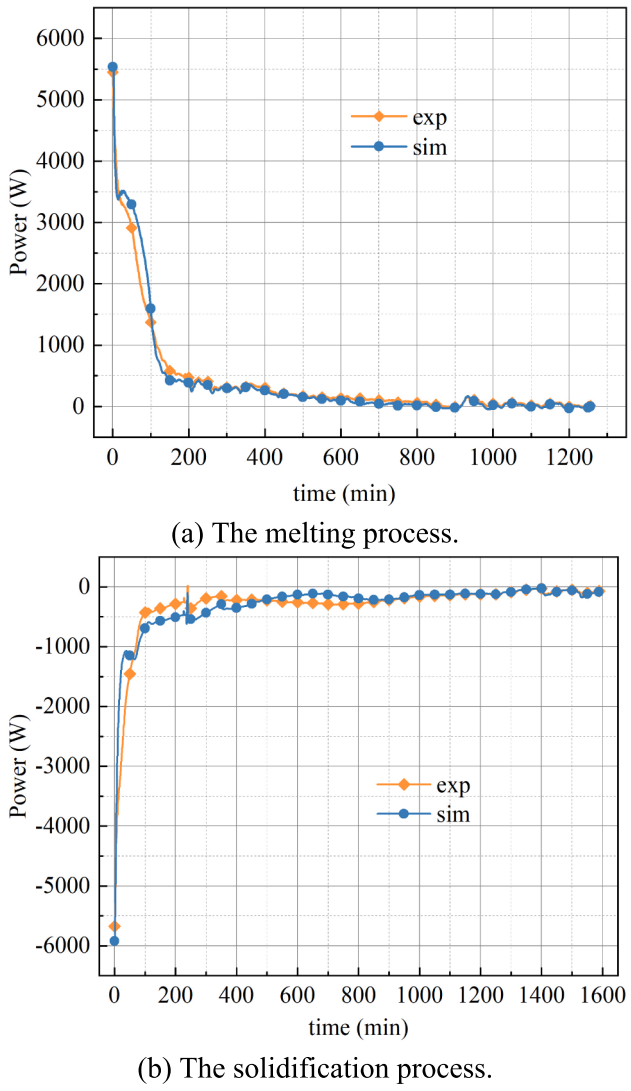

Fig. 10. The heat transfer power using the enthalpy method with the volume flow rate of 5 L/min.

which is determined by the control system of the data center. The HXCR can be used to evaluate the heat transfer power quickly if the storage temperature and state of charge are known. Thus, the HXCR is crucial for selecting the volume flow rate under the current system state and cooling requirements.

According to eq. (18), the average temperature of the PCM is necessary to calculate the HXCR, which is difficult to measure experimentally, but easy to obtain via numerical simulation. The state of charge is defined as the ratio of the thermal energy absorbed to the total heat capacity of the storage unit. The state of charge was used because the HXCRs of different volume flow rates can be compared on a fair basis.

Firstly, it shows that the HXCR increases with an increase in the volume flow rate at the same state of charge. This was because of the higher velocity of the water in the tubes. No slowdown in the increase in HXCR was observed with variations in the volume flow rates. However, further consideration is required when a larger volumetric flow rate is used because of the pressure drop.

Secondly, as shown in Fig. 17, the HXCR during the melting process dropped at the beginning, then remained constant, and dropped again. According to eq. (18), the HXCR depends on the ratio of the two

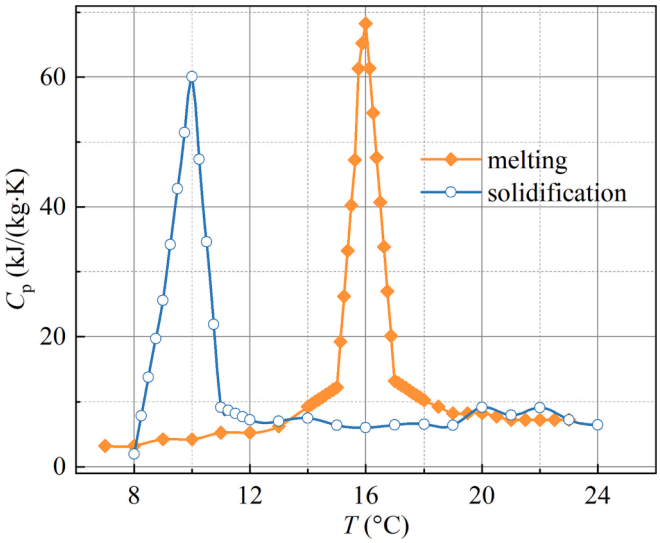

Fig. 12. Effective heat capacity used in the numerical model.

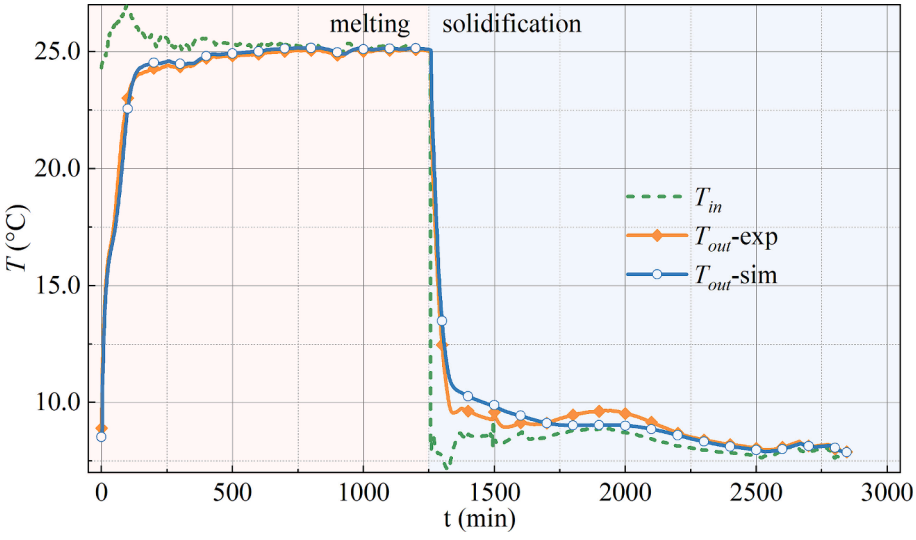

Fig. 11. The outlet temperature of the results of experiment and the effective heat capacity method with a flow rate of 5 L/min.

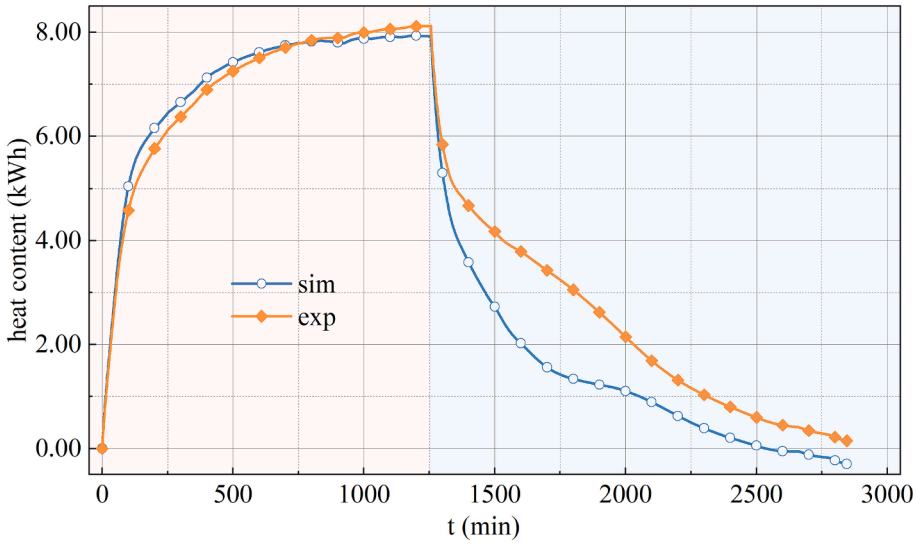

Fig. 13. The absorbed heat by the heat transfer using the effective heat capacity method with the flow rate of 5 L/min.

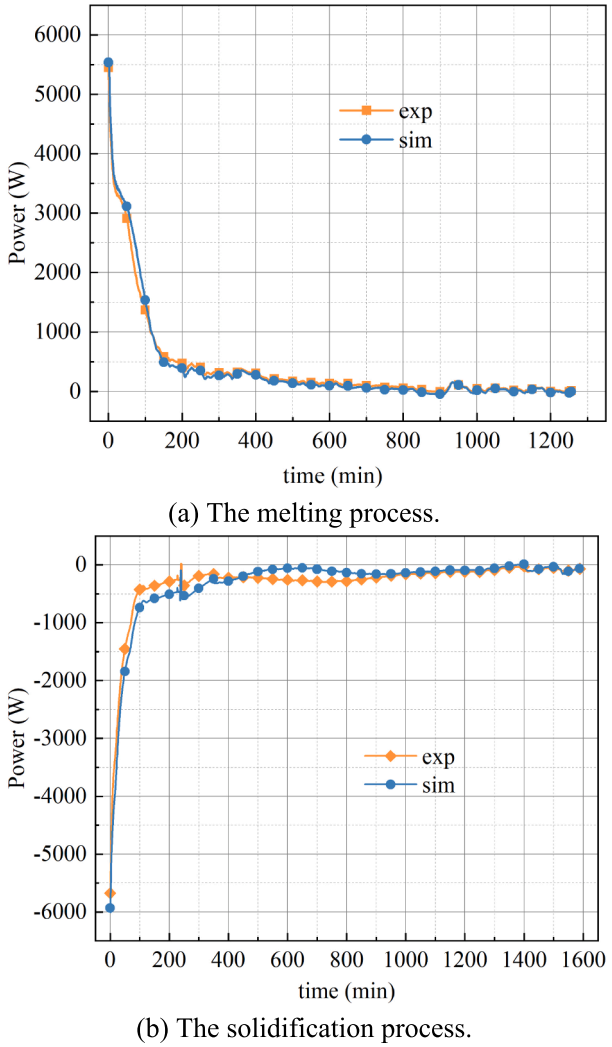

Fig. 14. The heat transfer power using the effective heat capacity method with the flow rate of 5 L/min.

differences: the difference between the inlet and outlet temperatures and the difference between the inlet temperature and the average temperature of the PCM. Initially, the temperature of the PCM increased more slowly than that of the water in the pipes, and the aforementioned ratio decreased. Subsequently, the PCM melted at the phase-change temperature, and the outlet temperature of the water was also stable. As a result, the HXCR maintained a constant value during this period. Finally, with an increase in the average temperature of the PCM, the ratio decreased, resulting in a decrease in the HXCR. Fluctuations were observed in the inlet temperature. When the charge status with a volume flow rate of 5 L/min was between 0.1 and 0.2, the inlet temperature increased consistently, resulting in an increase in the ratio mentioned above. Thus, the HXCR increases slightly during this period.

The HXCR decreased significantly towards the end of the melting process. During the last 50% of the process, the volume flow rate had a slight effect on the HXCR, as shown in Fig. 17. To achieve the desired heat transfer power and HXCR of the heat storage unit, it is beneficial to stop the melting and solidification processes before the heat transfer power or HXCR drops below a certain threshold. This technique can also be used to avoid supercooling because unmelt crystals serve as nucleation sites and trigger spontaneous solidification.

Table 5 lists the energy weighted HXCR with a variation of different state of charge. With the increase of the state of charge/discharge, the energy weighted HXCR decreased because of low heat transfer rate at the end of the melting or solidification process When the PCM melting as a 70% maximum capacity, the average HXCRs calculated by eq. (20) of the melting process reached 580 W/K with a 5 L/min flow, 690 W/K with a 10 L/min flow respectively.

5. Conclusions

Numerical models of latent heat storage for data center cooling were developed and validated against measurements. Two phase-change models, namely the enthalpy and effective heat capacity methods, were investigated. The optimized time step and under-relaxation factor were determined using a series of parameter studies. The outlet temperature, heat content of the storage unit, heat transfer power, and heat exchange capacity rate were determined for two different volume flow rates of the heat transfer fluid (5 and 10 L/min). The major conclusions are summarized as follows:

(1) The effective heat capacity method could satisfactorily predict the thermal performance of heat storage during the melting process. However, a significant deviation from the measurements

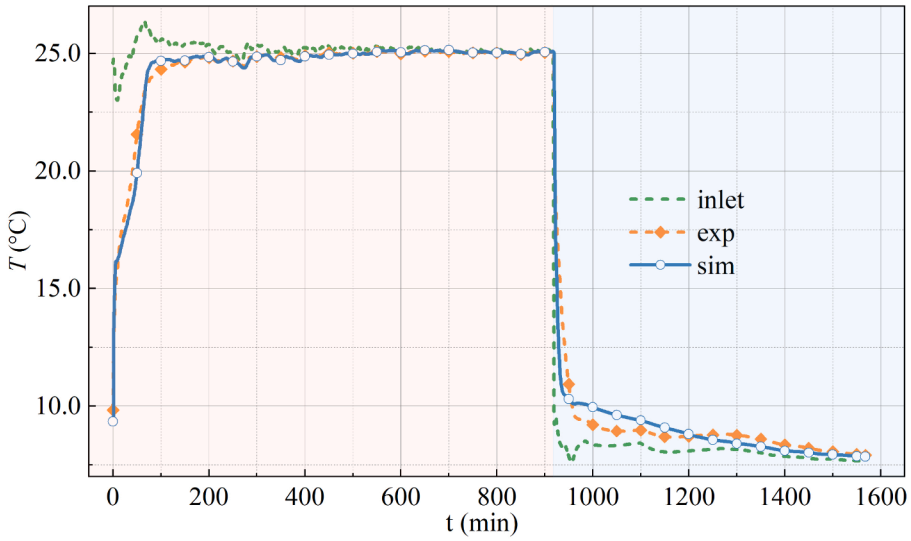

(a) The outlet temperature;

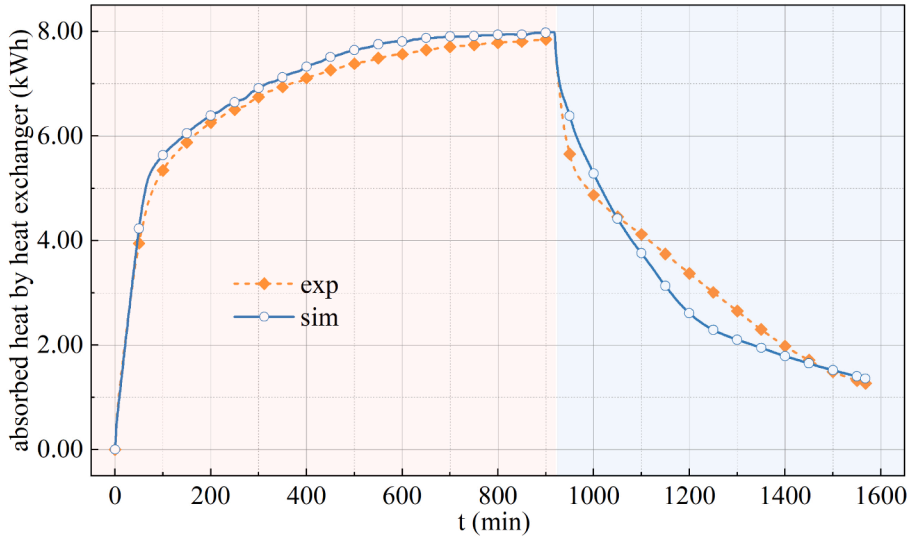

(b) The absorbed heat by the heat exchanger;

Fig. 15. The results of the enthalpy method and the experiment with a 10 L/min volume flow rate.

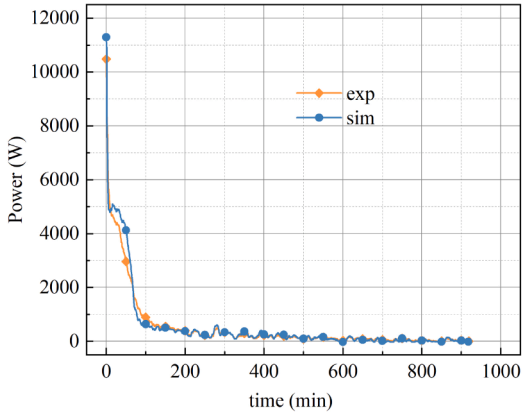

(a) The melting process;

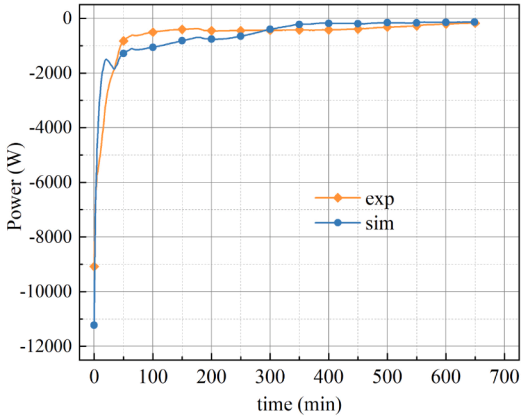

(b) The solidification process;

Fig. 16. The heat transfer power of the simulation and the experiment with the volume flow rate of 10 L/min.

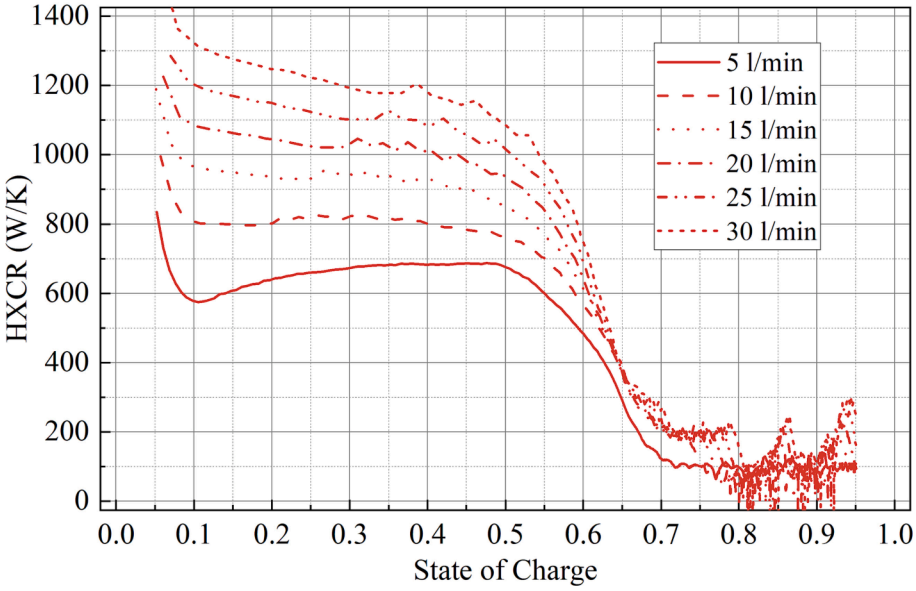

Fig. 17. The HXCR during the melting process with different volume flow rates.

Table 5
Energy weighted HXCR with different partial charge/discharge strategies.

		HXCR (W/K)			
State of Charge/Discharge		70%	80%	90%	95%
5 L/min	melting	580	527	475	455
	solidification	395	368	343	330
10 L/min	melting	690	613	553	528
	solidification	517	472	–	–

during the solidification process was observed. The heat absorbed by the heat exchanger, predicted using the enthalpy method, agreed well with that of the experiment during melting and solidification. Therefore, the enthalpy method is considered superior to the effective heat capacity method. Further modification of the effective heat capacity with the temperature is required to improve the agreement between the results.

(2) The water flow rate affects heat transfer. An increase in the water volume flow rate from 5 to 10 L/min increased the average heat transfer power by 47 and 59% for melting and solidification processes. The melting and solidification times were reduced by 338 min and 311 min, respectively.

(3) The energy-weighted heat exchange capacity rate during the solidification process was lower than that during the melting process because of the small temperature difference. This is because of the smaller temperature difference for heat transfer caused by supercooling. An increase in the volume flow rate increases the heat exchange capacity rate during the melting process. However, the effect becomes slight at the final 50% process. Thus, working at a partial capacity is helpful for increasing the heat transfer performance. Compared with the case working as 95% of full capacity, the average heat exchange capacity rate of the melting process increased by 27.5% with a 5 L/min flow, 30.7% with a 10 L/min flow respectively.

Declaration of Competing Interest

The authors declare that they have no known competing financial interests or personal relationships that could have appeared to influence the work reported in this paper.

Data availability

Data will be made available on request.

Acknowledgement

This work was co-financed by the Innovation Fund Denmark project titled 'Cool-Data Flexible Cooling of Data Centers' (No. 0177-00066B). The Chinese Scholarship Council (CSC) (No. 202106120167) also partly funded this research. Without their support, this study would have been impossible.

References

[1] International Renewable Energy Agency, Innovation outlook thermal energy storage, (2020). www.irena.org.
[2] International Energy Agency, Next Generation Wind and Solar Power - From Cost to Value, (2016). www.iea.org/t&c/.
[3] Z. Ma, X. Wang, P. Davenport, J. Gifford, J. Martinek, Economic Analysis of a Novel Thermal Energy Storage System Using Solid Particles for Grid Electricity Storage: Preprint, (2021). https://www.nrel.gov/docs/fy21osti/79014.pdf.
[4] SunShot Vision Study, (2012). https://doi.org/10.2172/1039075.
[5] Z. Zhou, Z. Zhang, J. Zuo, K. Huang, L. Zhang, Phase change materials for solar thermal energy storage in residential buildings in cold climate, Renew. Sustain. Energy Rev. 48 (2015) 692–703, https://doi.org/10.1016/j.rser.2015.04.048.
[6] E. Guelpa, V. Verda, Thermal energy storage in district heating and cooling systems: A review, Appl. Energy 252 (2019), 113474, https://doi.org/10.1016/j.apenergy.2019.113474.
[7] S. Bourne, A. Novoselac, Compact PCM-based thermal stores for shifting peak cooling loads, Build. Simul. 8 (2015) 673–688, https://doi.org/10.1007/s12273-015-0243-6.
[8] M. Dannemand, J.B. Johansen, W. Kong, S. Furbo, Experimental investigations on cylindrical latent heat storage units with sodium acetate trihydrate composites utilizing supercooling, Appl. Energy 177 (2016) 591–601, https://doi.org/10.1016/j.apenergy.2016.05.144.
[9] G. Englmair, C. Moser, S. Furbo, M. Dannemand, J. Fan, Design and functionality of a segmented heat-storage prototype utilizing stable supercooling of sodium acetate trihydrate in a solar heating system, Appl. Energy 221 (2018) 522–534, https://doi.org/10.1016/j.apenergy.2018.03.124.
[10] G. Wang, C. Xu, G. Englmair, W. Kong, J. Fan, S. Furbo, G. Wei, Experimental and numerical study of a latent heat storage using sodium acetate trihydrate for short and long term applications, J Energy Storage. 47 (2022), 103588, https://doi.org/10.1016/j.est.2021.103588.
[11] S. Zhang, L. Pu, S. Mancin, M. Dai, L. Xu, Role of partial and gradient filling strategies of copper foam on latent thermal energy storage: An experimental study, Energy 255 (2022), 124517, https://doi.org/10.1016/j.energy.2022.124517.
[12] X.Q. Zhai, X.W. Cheng, C. Wang, R.Z. Wang, Experimental investigation and performance analysis of a fin tube phase change cold storage unit for high temperature cooling application, Energ. Buildings 89 (2015) 9–17, https://doi.org/10.1016/j.enbuild.2014.12.021.

[13] H. Behi, M. Behi, A. Ghanbarpour, D. Karimi, A. Azad, M. Ghanbarpour, M. Behnia, Enhancement of the thermal energy storage using heat-pipe-assisted phase change material, Energies (Basel). 14 (2021) 6176, https://doi.org/10.3390/en14196176.
[14] X. Gao, P. Wei, J. Yu, X. Huang, X. Yang, B. Sundén, Design and assessments on graded metal foam in heat storage tank: An experimental and numerical study, Int. Commun. Heat Mass Transfer 146 (2023), https://doi.org/10.1016/j.icheatmasstransfer.2023.106902.
[15] C. Li, Q. Li, R. Ge, Comparison of performance enhancement in a shell and tube based latent heat thermal energy storage device containing different structured fins, Renew, Energy 206 (2023) 994–1006, https://doi.org/10.1016/j.renene.2023.02.087.
[16] R. Waser, F. Ghani, S. Maranda, T.S. O'Donovan, P. Schuetz, M. Zaglio, J. Worlitschek, Fast and experimentally validated model of a latent thermal energy storage device for system level simulations, Appl. Energy 231 (2018) 116–126, https://doi.org/10.1016/j.apenergy.2018.09.061.
[17] M. Zálešák, P. Charvát, L. Klimeš, Identification of the effective heat capacity–temperature relationship and the phase change hysteresis in PCMs by means of an inverse heat transfer problem solved with metaheuristic methods, Appl. Therm. Eng. 197 (2021), 117392, https://doi.org/10.1016/j.applthermaleng.2021.117392.
[18] W. Kong, G. Wang, G. Englmair, E.N.N. Nielsen, J. Dragsted, S. Furbo, J. Fan, A simplified numerical model of PCM water energy storage, J Energy Storage. 55 (2022), 105425, https://doi.org/10.1016/j.est.2022.105425.
[19] R. Waser, S. Maranda, A. Stamatiou, M. Zaglio, J. Worlitschek, Modeling of solidification including supercooling effects in a fin-tube heat exchanger based latent heat storage, Sol. Energy 200 (2020) 10–21, https://doi.org/10.1016/j.solener.2018.12.020.
[20] S. Lu, Q. Lin, Y. Liu, L. Yue, R. Wang, Study on thermal performance improvement technology of latent heat thermal energy storage for building heating, Appl. Energy 323 (2022), 119594, https://doi.org/10.1016/j.apenergy.2022.119594.
[21] Z. Liu, Z. Liu, G. Liu, X. Yang, J. Yan, Melting assessment on the effect of nonuniform Y-shaped fin upon solid–liquid phase change in a thermal storage tank, Appl. Energy 321 (2022), 119330, https://doi.org/10.1016/j.apenergy.2022.119330.
[22] A.H. Eisapour, A.H. Shafaghat, H.I. Mohammed, M. Eisapour, P. Talebizadehsardari, A. Brambilla, A.S. Fung, A new design to enhance the conductive and convective heat transfer of latent heat thermal energy storage units, Appl. Therm. Eng. 215 (2022), 118955, https://doi.org/10.1016/j.applthermaleng.2022.118955.
[23] J. Wołoszyn, K. Szopa, A combined heat transfer enhancement technique for shell-and-tube latent heat thermal energy storage, Renew, Energy 202 (2023) 1342–1356, https://doi.org/10.1016/j.renene.2022.12.010.
[24] M. Fan, Z. Luan, H. Yang, X. Zhang, M. Hou, L. Guo, X. Kong, Charging and discharging characteristics of cascaded latent heat storage (CLHS) tank for low-temperature applications, Appl. Therm. Eng. 213 (2022), 118698, https://doi.org/10.1016/j.applthermaleng.2022.118698.
[25] M. Iten, S. Liu, A. Shukla, Experimental validation of an air-PCM storage unit comparing the effective heat capacity and enthalpy methods through CFD simulations, Energy 155 (2018) 495–503, https://doi.org/10.1016/j.energy.2018.04.128.
[26] S. Chen, C. Yu, G. Wang, W. Kong, Z. Tian, J. Fan, Heat transfer of a shell and tube sodium acetate trihydrate heat storage tank, J Energy Storage. 55 (2022), 105600, https://doi.org/10.1016/j.est.2022.105600.
[27] P. Huang, B. Copertaro, X. Zhang, J. Shen, I. Löfgren, M. Rönnelid, J. Fahlen, D. Andersson, M. Svanfeldt, A review of data centers as prosumers in district energy systems: Renewable energy integration and waste heat reuse for district heating, Appl. Energy 258 (2020), 114109, https://doi.org/10.1016/j.apenergy.2019.114109.
[28] X. Yuan, X. Zhou, Y. Pan, R. Kosonen, H. Cai, Y. Gao, Y. Wang, Phase change cooling in data centers: A review, Energ. Buildings 236 (2021), 110764, https://doi.org/10.1016/j.enbuild.2021.110764.
[29] M. Wahlroos, M. Pärssinen, J. Manner, S. Syri, Utilizing data center waste heat in district heating – Impacts on energy efficiency and prospects for low-temperature district heating networks, Energy 140 (2017) 1228–1238, https://doi.org/10.1016/j.energy.2017.08.078.
[30] L. Liu, Q. Zhang, Z. (John) Zhai, C. Yue, X. Ma, State-of-the-art on thermal energy storage technologies in data center, Energy Build. 226 (2020) 110345. https://doi.org/10.1016/j.enbuild.2020.110345.
[31] X. Ma, Q. Zhang, S. Zou, An experimental and numerical study on the thermal performance of a loop thermosyphon integrated with latent thermal energy storage for emergency cooling in a data center, Energy 253 (2022), 123946, https://doi.org/10.1016/j.energy.2022.123946.
[32] B. Huang, Z. Zheng, G. Lu, X. Zhai, Design and experimental investigation of a PCM based cooling storage unit for emergency cooling in data center, Energ. Buildings 259 (2022), 111871, https://doi.org/10.1016/j.enbuild.2022.111871.
[33] Y. Fang, J. Niu, S. Deng, Optimizing LHS system using PCM in a tube-in-tank design for emergency cooling, in: Energy Procedia, (2017) 3381–3387. https://doi.org/10.1016/j.egypro.2017.12.474.
[34] Z. Zheng, B. Huang, G. Lu, X. Zhai, Design and optimization of an air-based phase change cold storage unit through cascaded construction for emergency cooling in IDC, Energy 241 (2022), 122897, https://doi.org/10.1016/j.energy.2021.122897.
[35] S.P. Venkateshan, Mechanical Measurements, 2 nd Edition, (2015).
[36] Kamstrup, smart water meters & devices. https://www.kamstrup.com/en-us/water-solutions/smart-water-meters.
[37] Ansys, Ansys Fluent User's Guide, (2022). http://www.ansys.com.
[38] Rubitherm, Technical data sheet, Rubitthermal Technologies GmbH, 2022. https://www.rubitherm.eu/media/products/datasheets/Techdata_-SP15_gel_EN_12072022.PDF.
[39] DTU Computing Center, DTU Computing Center resources, (2022). https://doi.org/10.48714/DTU.HPC.0001.
[40] Ansys Fluent Theory Guide, 2022. http://www.ansys.com.
[41] M. Fadl, P.C. Eames, Numerical investigation of the influence of mushy zone parameter Amush on heat transfer characteristics in vertically and horizontally oriented thermal energy storage systems, Appl. Therm. Eng. 151 (2019) 90–99, https://doi.org/10.1016/j.applthermaleng.2019.01.102.
[42] Y. Hu, R. Guo, P.K. Heiselberg, H. Johra, Modeling pcm phase change temperature and hysteresis in ventilation cooling and heating applications, Energies (Basel). 13 (2020), https://doi.org/10.3390/en13236455.
[43] I.B. Celik, U. Ghia, P.J. Roache, C.J. Freitas, H. Coleman, P.E. Raad, Procedure for estimation and reporting of uncertainty due to discretization in CFD applications, Journal of Fluids Engineering, Transactions of the ASME. 130 (2008) 0780011–0780014, https://doi.org/10.1115/1.2960953.